Cellulose (2023) 30:6173–6185
https://doi.org/10.1007/s10570-023-05290-w

ORIGINAL RESEARCH

Air-drying of 3D printed part made of ligno-cellulosic fibres: 3D real-time monitoring combining sub-minute laboratory X-ray microtomography and digital volume correlation

H. Murtaza · S. Rolland du Roscoat · P. Lhuissier · L. Salvo · L. Orgéas · C. Thibaut · A. Denneulin · D. Chaussy · D. Beneventi

Received: 14 October 2022 / Accepted: 24 May 2023 / Published online: 8 June 2023

Abstract 3D cheap, lightweight and robust cellulosic parts can be obtained via extrusion of a cellulosic aqueous paste followed by air-drying. During the air-drying step, an anisotropic shrinkage occurs. The objective of this study is to characterize the macro and mesoscale phenomena occurring during the drying process. We used sub-minute laboratory X-ray microtomography during air-drying tests combined with advanced image analysis including Digital Volume Correlation to reveal the mechanisms that took place at the sample and at the filament scales. This allowed the qualitative and quantitative analysis of the structural and kinematical changes occurring during the air-drying. The macroscopic anisotropic shrinkage of the structure is associated with a decrease of the solid fraction of the cube and a decrease of the volume of the central pore, a decrease of the number and of the volume of the inter-filament and intra-filament pores, a change of the shape and dimensions of the filaments cross section. We observed delamination effects, increase of the number of inter and intra filament pores. These results complete the analysis commonly carried out at the macroscale and are necessary to build a model for the prediction of drying mechanisms of 3D printed part of cellulose and to propose more accurate compensation strategies.

Keywords 3D printing by extrusion · Air drying · Cellulose paste · X-ray microtomography · Digital volume correlation

H. Murtaza · S. Rolland du Roscoat (✉) · L. Orgéas · C. Thibaut
Université Grenoble Alpes, CNRS, Grenoble INP (Institute of Engineering Université Grenoble Alpes), 3SR, 38000 Grenoble, France
e-mail: sabine.rollandduroscoat@3sr-grenoble.fr

H. Murtaza · P. Lhuissier · L. Salvo
Université Grenoble Alpes, CNRS, Grenoble INP (Institute of Engineering Université Grenoble Alpes), SIMAP, 38000 Grenoble, France

C. Thibaut · A. Denneulin · D. Chaussy · D. Beneventi
Université Grenoble Alpes, CNRS, Grenoble INP (Institute of Engineering Université Grenoble Alpes), LGP2, 38000 Grenoble, France

Introduction

In the last decade, additive manufacturing technologies, commonly named 3D printing, of cellulose based polymer have been increasingly developed for various applications such as medical or electronical because cellulose is a very promising candidate to produce cheap, lightweight, robust, and recyclable 3D structures by 3D printing (Wang et al. 2018; Dai et al. 2019; Firmanda et al. 2021). Despite the fact that lignocellulosic fibres represent the most abundant bio-based polymer on Earth and present excellent mechanical properties (Dufresne 2017), the use of cellulose in the form of short fibers or microfibrils or nanofribrils in the specific case of additive

manufacturing by material extrusion is still in its early stages (Markstedt et al. 2014; Wang et al. 2018). Namely, pastes made up of short ligno-cellulosic fibers contain a large amount of water (larger than 50%wt, Thibaut et al. 2019) which induce important and heterogeneous shrinkage (larger than 30%) upon air-drying (Klar et al. 2017). In such processes, the huge strains undergone by the object come from an interplay between gravity, water evaporation and capillary effects which mainly occurs during the first hours of drying (Rémond et al. 2010; Sampson and Yamamoto 2011) with typically 3 temporal phases. Phase I corresponds to a constant drying rate period during which the water evaporation at the surface of the sample is replaced by water diffusion, *i.e*. the rate of evaporation is of the same order of magnitude as the rate of water diffusion inside the sample. Phase II corresponds to the falling rate period during which the surface water evaporation is not fast enough to maintain a continuous water film onto the sample surface. Phase III corresponds to a steady state regime where an equilibrium is reached and another constant drying rate is observed (Scherer 1990; Thiery et al. 2017; Zhou et al. 2019; Tang and Min 2019). In the case of cellulose part obtained by 3D printing and air-dried, these drying 3 main drying phases occur; as a consequence of the drying induces the final geometry and the inner structure of the extruded filaments as well as their contacts created during the printing process, and thus the final geometry of the dried final part.

In order to understand and to quantify the microstructural changes occurring at various scales (part or filament) during air-drying of cellulose paste and to link these microstructural modifications with the final shape of the 3D printed part, there is a need to visualize, in real time and in 3D, the 3D structure at the filament scale during drying (Metzger 2019). Among the tools to be used purposely, X-ray microtomography has been successfully used to visualize (Huan et al. 2018; Pfister et al. 2004) and characterize the final shapes and mesostructures of such 3D printed structures made up of cellulose (Klar et al. 2019). However, none of these works proposed a temporal 3D characterization of the samples during the air-drying process. This monitoring has already been performed using synchrotron X-ray tomography in the case of hydro-mechanical tests on ligno-cellulosic materials (Joffre et al. 2016; Viguie et al. 2011) or during 3D printing of metallic part (Lhuissier et al. 2020), with high-quality 3D images recorded in a second or less, thus allowing unprecedented temporal 3D quantitative analysis of microstructural evolutions. Based on the recent protocol developed recently for laboratory X-ray tomographs (Dewanckele et al. 2020), we could study the air drying of a 3D printed part produced by extrusion of a short lingo-cellulosic fiber based paste with 3D real-time in situ observations coupled with a 3D quantitative analysis. Doing so, we could characterize quantitatively the evolution of the structural and kinematical changes induced during three main phases of the drying process, at the printed part scale but also at the filament scale. This quantification was also related to standard measurements.

Material and methods

3D Printed cellulose sample: Preparation

One 9^3 mm^3 cube with an inner 3D grid (Fig. 1a) was printed using an optimized aqueous cellulose-based paste with 40% w/w dry solid content (Thibaut et al. 2019) made up of (i) carboxymethyl cellulose (Fig. 1b) with a molecular weight of 90,000 $g.mol^{-1}$ and a substation degree of 0.7 carboxymethyl groups per anhydroglucose unit and (ii) of short ligno-cellulosic fibers (Fig. 1c) provided by Carl Roth. The fibers consisted of a mix of milled hardwood and softwood; 90% of the fibers were shorter than 200 µm. More details can be found in (Thibaut et al. 2019). The used commercial printer was Prusa i3 upgraded with a liquid deposit modelling (LDM) WASP extruder. The used nozzle had an exit diameter of 0.72 mm. The printing settings specified in the slicing software (Simplify 3D) were as follow: an extrusion width of 0.71 mm, a layer height of 0.45 mm, 2 perimeters shells, a 50% infill with rotation between 0° and 90° angles at every layer, an outline overlap of 60%. The printing speed was 10 mm s^{-1} leading to a printing time of about 3 min. The printed cube (Fig. 1d) was dried at the room temperature at 22 ± 2 °C and 30 ± 3% of relative humidity (Fig. 1e). In the following, x and y refer to the two main in-plane directions of printing whereas z refers to the thickness of the part, as illustrated in Fig. 1a.

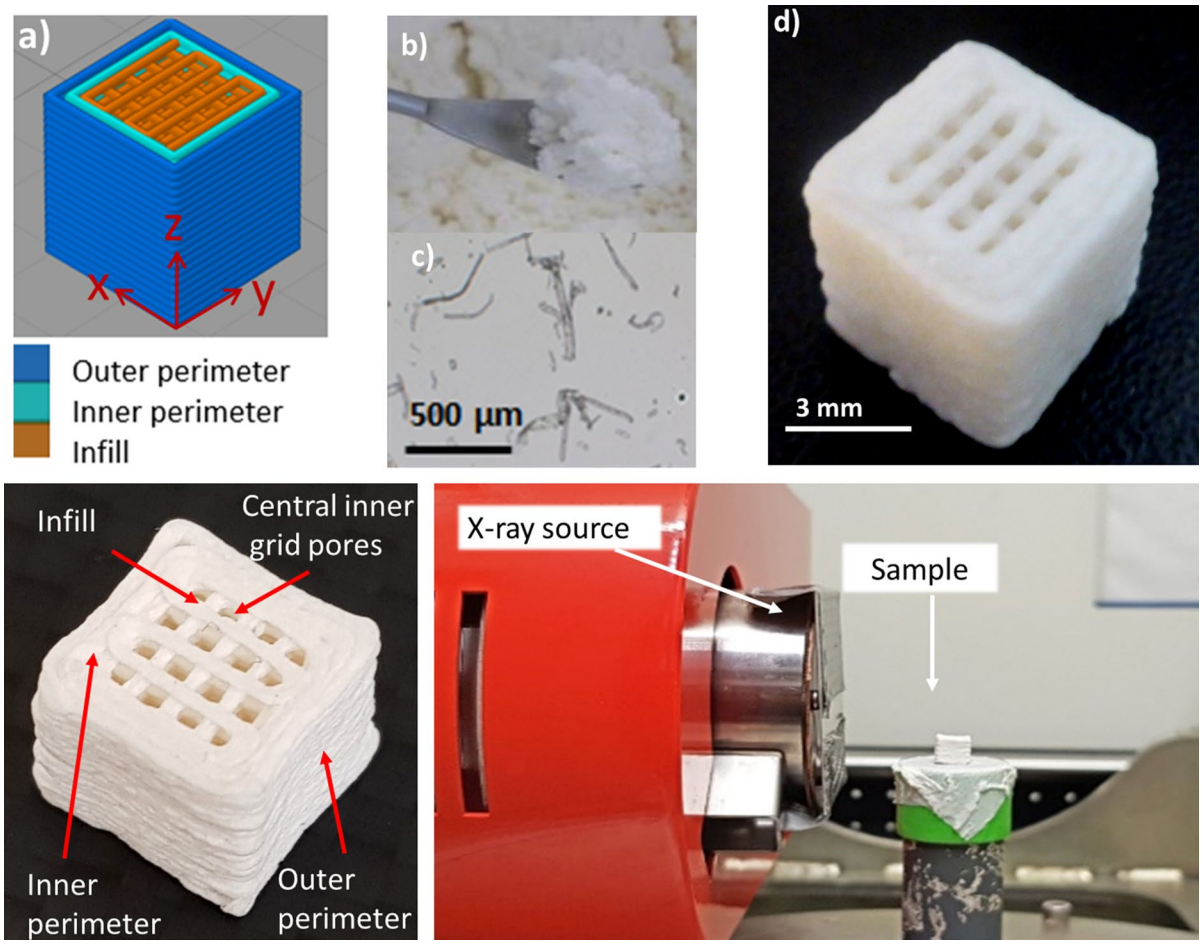

Fig. 1 **a** 3D STL model of 3D cube to be printed. **b** Aqueous carboxymethyl cellulose (CMC); **c** Natural ligno-cellulosic fibers in suspension; **d** Freshly 3D printed cube; **e** 3D printed air dried cube; **f** Sample placed in the laboratory X-ray micro-tomograph

Sub-minute laboratory X-ray micro tomography

The monitoring of the drying process of the printed part was performed using the RX Solutions microtomograph located in 3SR laboratory (Fig. 1f). The image acquisition protocol was optimized in order to achieve a scanning time of only 36 s, which is compatible with the time scale necessary to capture the dynamic material response upon drying (Thibaut et al. 2019). For that purpose, the X-ray tube (Hamamatsu Corporation L8121-03 X-ray sealed source) was operated in middle focal spot mode at power of 30 W with an acceleration voltage of 100 kV and a filament current of 300 µA. A 0.5 mm thick Aluminum filter was also placed in front of the X-ray source to eliminate the lower energy photons. In addition, the detector was an "indirect" flat-panel Varian PaxScan® 2520. It has the capacity to measure the intensity of incident X-ray photons on an array of 1920×1536 pixels, with each pixel measuring 127×127 µm^2. The flat-panel Varian was set in binning 4 mode with a frame rate of 60 Hz and an average of 3 frames, resulting in the acquisition of 20 radiographs of 480×384 pixels per second. Moreover, the distance between the source and the sample was set to 42 mm, and the distance between the sample and the detector was 724 mm. The samples were scanned with a magnification 18.2 resulted in a voxel size of 28^3 µm^3. Lastly, 720 radiographs were recorded over 360 degrees with an acquisition time of 36 s in continuous rotation mode of the rotating stage. Scans were recorded every 4 min during 8 h, leading to a total of 120 scans.

Data processing and analysis

Pre-processing

The 3D images were reconstructed from the 2D radiographs using filtered back projection algorithm implemented by RX solutions. Figure 2a shows a typical vertical slice obtained after reconstruction, thus proving the good quality of the acquired 3D images, in spite of the very short scanning time used to get them. They were used to analyse kinematical fields (§ 2.1.3). For structural characterization (§ 2.1.2), the images were also segmented using a thresholding operation to distinguish the porous phase from the solid one. The same threshold was applied to the 120 scans (Fig. 2b). It was obtained by averaging the threshold values found for the 120 scans. The chosen segmentation method is the auto threshold function provided by the freeware ImageJ. The final binarized volumes were cropped (Fig. 2c) to facilitate the post-processing and to remove the noise that can be observed in the first printed layers due to shadowing of the base plate (Fig. 2d). Figure 2e shows the working 3D image of the solid phase used to perform the quantitative analysis.

Structural analysis

The volume of each phase was computed by multiplying the total number of voxels belonging to each phase by the voxel size. Thus, we could estimate the intrinsic volumetric strain of the solid phase $\varepsilon_v^i = \ln(V_s/V_{s0})$, where V_s and V_{s0} are the volume of the solid phase in the actual and initial configuration, respectively. In addition, the pores were identified by labelling the porous phase using the Analysis 3D plugin of ImageJ (Boulos et al. 2012). It labelled the 3D connected components with a specified connectivity of 26 neighbours. Once identified, the volume V and the surface area A of each pore were computed using a marching cube algorithm. Pores that exhibited a volume smaller than 30 voxels (6.58×10^{-4} mm^3) were discarded as well as most of these pores come from the threshold sensitivity. The sphericity S of the pores was evaluated using $S = 6V(\frac{\pi}{A^3})^{0.5}$ (Boulos et al. 2012), which ranges from

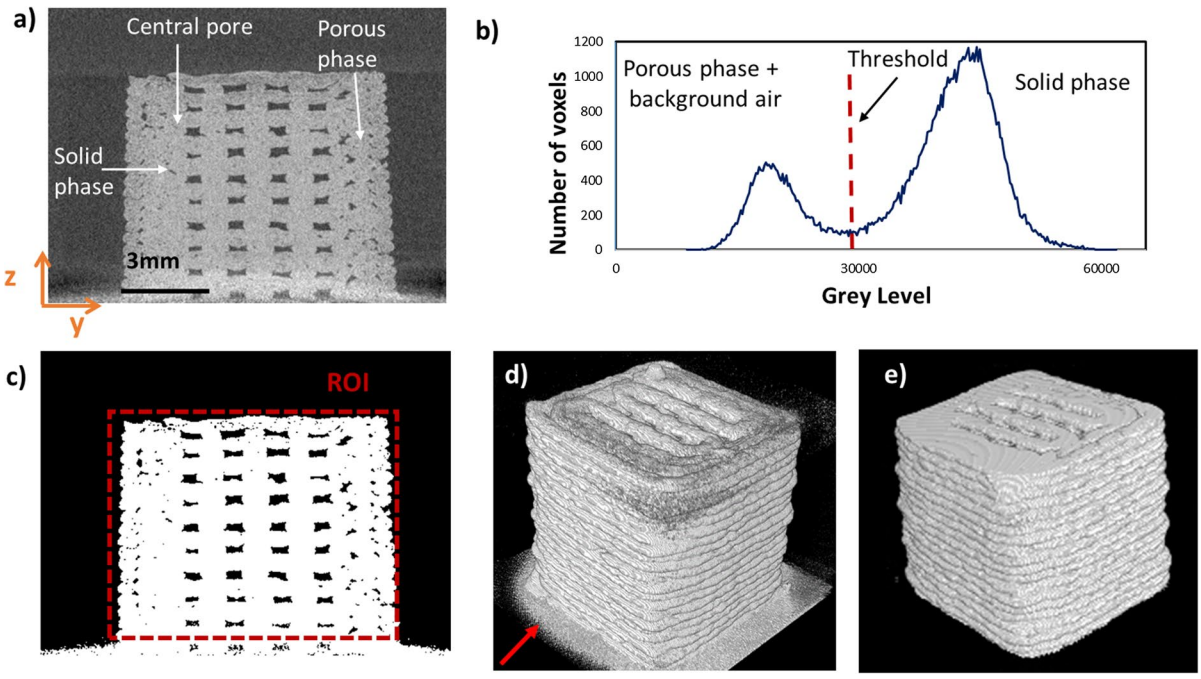

Fig. 2 **a** Vertical slice of a 3D reconstructed image showing the cube inner structure with porous and solid phases. **b** Histogram of reconstructed volume showing the cut-off threshold used to segment the phases. **c** Binarized version of the vertical slice (a), with the region of interest (ROI) marked in dashed red lines. **d** 3D view of the original binarized volume (solid phase). **e** 3D view of working volume

0 and 1 when switching from elongated or tortuous pores to spherical pores, respectively.

Kinematics analysis

Displacement fields and associated strain fields In order to study the deformation mechanisms occurring during shrinkage induced by the drying of the cube at the cube and the filament scales, the 3D Digital Volume Correlation (DVC) technique implemented in the SPAM freeware was used (Stamati et al. 2020). This technique allows getting the displacement between two grey intensity images obtained from two consecutives 3D images (Viguie et al. 2011, Stamati et al. 2020) in order to get 3D displacement and strain fields. We first used the whole images as correlation windows in order to get the macroscopic strain field, *i.e.* the strain field at the cube scale. In order to assess the mesoscale strain field, *i.e.*, at the filament scale, we also used correlation windows with a size of 6^3 voxels centred around measurement points of a 3D regular orthogonal grid (node spacing 4 voxels). We computed the volumetric strain $\varepsilon_v = \ln(\det \mathbf{F})$ as well as the macroscale (resp. mesoscale) Hencky strain tensor $\boldsymbol{\varepsilon}$, where $\mathbf{F}$ is the macroscale (resp. mesoscale) gradient of the geometrical transformation deduced from the macroscale (resp. mesoscale) displacement fields.

Pores Tracking To monitor the morphological evolution and the kinematics of pores during the drying period, the centres of mass of some labelled pores (§ 2.1.2) were individually tracked using SPAM over the multiple scans. Data position of computed and an estimate of this position in the successive scans were obtained using the field provided by the DVC. Matching was performed step by step by comparison of the estimated position in previous step and positions in current step. To validate the procedure, we checked for some pores that the manual tracking gave the same results.

Results

Macroscale analysis

Figure 3 shows the 3D cross-sectional views of the imaged sample at increasing drying time t. An important macroscopic shrinkage in the early stages of drying ($t \ll 240$min) is observed. It is less pronounced but still here at higher drying times $t = 240$ min. This shrinkage exhibited anisotropy as it occurred mainly along the sample height (z direction). It was accompanied with microstructural changes such as crack initiation and propagation which did not affect the outer part of the sample. Moreover, we cannot observe any collapse of the structure. This is due to the rheological behaviour of the paste (Thibaut et al. 2019; Chalencon et al. 2010), which corresponds to the requirements of the 3D printing by extrusion, i.e. a high level of yield stress of the paste rheology.

To better quantify this drying induced shrinkage, we have reported in Fig. 4 the time-evolutions of the macroscopic ε_v and intrinsic ε_v^i volumetric strains (Fig. 4a) as well as the macroscopic strain components evolution of strain in the principal directions ε_{xx}, ε_{yy} and ε_{zz} (Fig. 4b). These graphs show that whatever the considered strain measure, the

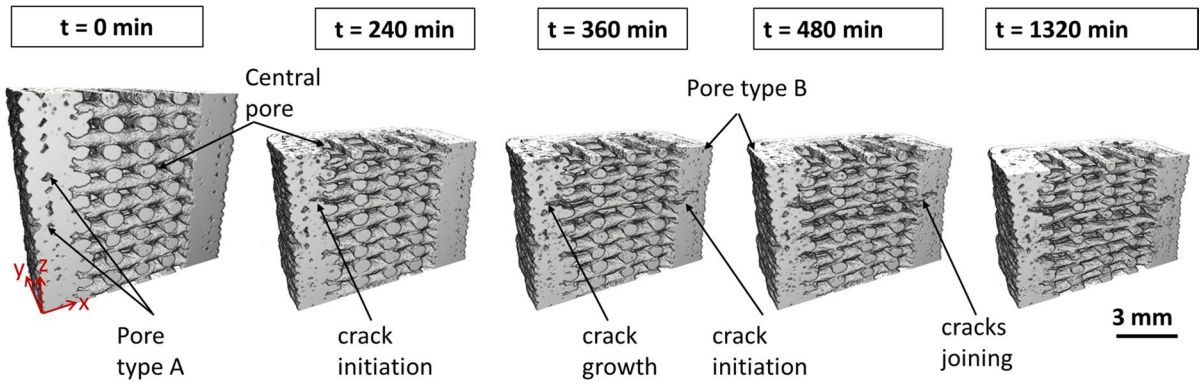

Fig. 3 3D rendered cross-sectional view of reconstructed X-ray tomographic scans at different drying time t

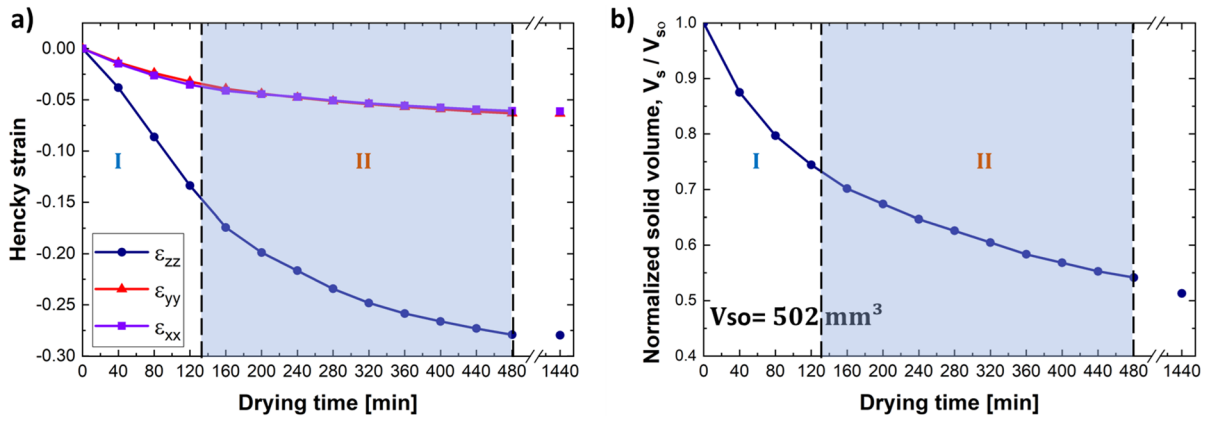

Fig. 4 **a** Time-evolutions of (**a**) the macroscopic and intrinsic volumetric strain (**a**) and Hencky strains ε_{xx}, ε_{yy} and ε_{zz} (**b**)

time-evolution can be split in three regions: a first sharp decrease characterizing an important shrinkage for times below 120 min (zone I), a "steady sate" regime above 480 min within which strains are practically constant (zone III), and a transition zone II between the two aforementioned zones. These time evolutions are in-line with those observed in the literature (Scherer 1990; Thiery et al. 2017; Zhou et al. 2019, Tang et Min 2019, e.g.).

Figure 4a shows that the solid phase is subjected to a substantial shrinkage, as the intrinsic volumetric strain ε_v^i is close to -67% at the end of the experiment. Albeit lower, this value is consistent with results reported in (Thibaut 2020) and with the theoretical volume of the solid phase after complete water removal, *i.e.*, − 71%. The discrepancy between the measured and calculated strains can be associated with (i) the presence of ca. 20% w/w residual water in the filaments whose removal requires a harsh thermal treatment and (ii) the possible errors induced by the segmentation and the spatial resolution of the 3D images. It is worth noticing that the macroscale volumetric strain ε_v is much lower than the intrinsic one ε_v^i. For example, at the end of the experiment, ε_v only reached − 38% whereas ε_v^i is close to − 67%. This difference is ascribed to the heterogeneous geometry of the studied sample: during drying local shrinkage zone can occur, *e.g.*, the cracks shown in Fig. 3, without altering the macroscale deformation of the samples.

The Fig. 4b highlights the marked anisotropy of the sample shrinkage. The transverse macroscale strains ε_{xx} and ε_{yy} are practically identical and reach a value close to − 5% at the end of the experiment due to the symmetry of the structure. On the opposite, the vertical shrinkage ε_{zz} is much higher and reaches a value close to − 27%. This difference is similar to those obtained in other studies (Thibaut et al. 2019; Huan et al. 2018). A first contribution to this anisotropy is related to the anisotropic drying of the single filaments, which (i) are all aligned along the (x, y) plane and (ii) exhibits larger shrinkage strain along their diameter than along their length (Thibaud et al. 2019), due to the marked alignment of the ligno-cellulosic fibre along the filament direction (Wainwright et al. 1982). Another contribution is related to gravity forces which may induce a sample height reduction, especially during the early stage of the drying when the paste can still flow/creep.

Mesoscale analysis

Figure 5a shows 3D views of the local incremental volumetric strain $\Delta\varepsilon_v$ obtained by correlating two data sets for t and t+20 min. Figure 5b and c do the same but in the (y,z) and (x,y) planes shown in Fig. 5a, respectively.

These figures show that for **t** = 0–20 min and for **t** = 40–60 min**:** the local volumetric strains are mainly negative with volumetric strains decreasing down to − 0.15. It is interesting to note that these highest negative values are located on the external surfaces of the sample which are where moisture transport is facilitated due to the high surface contact with air (Thiery et al. 2017, Zhou et al. 2019, Tang et Min 2019). We can also notice larger local negative volumetric strain

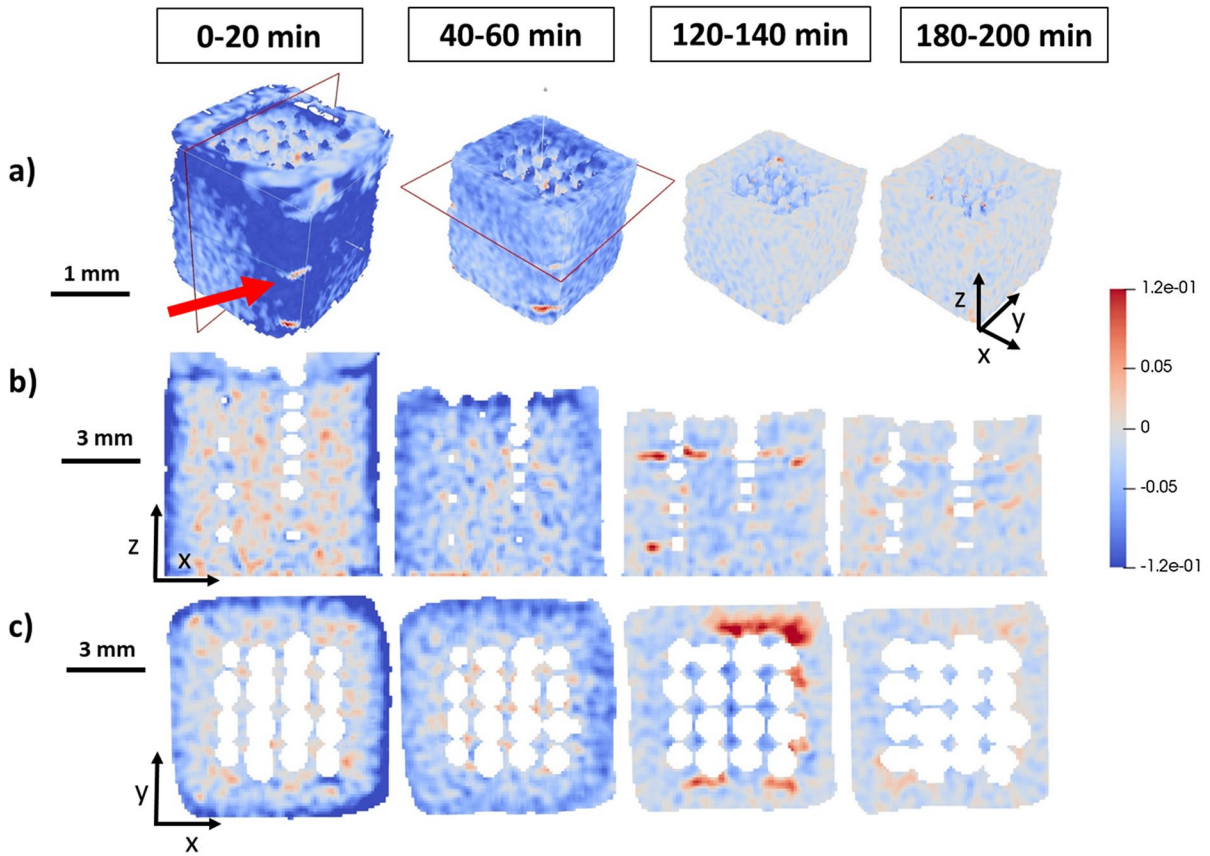

Fig. 5 **a** Temporal evolution of the volumetric strain field a) 3D views, **b** vertical cross section **c** horizontal cross section of the plans indicate on a). The red arrow indicates the side of the cube located close to the X-ray source

on one face compared to the other one (Fig. 5a). This may be due to faster drying of the side of the cube located closed to the X-ray source. Namely, to stabilise it, the X-ray source was not switched off during the waiting time between two scans. This induced a temperature of 36 °C inside the X-ray source and an estimated temperature gradient around the sample of 3 °C/cm. This higher temperature induced upon drying some filaments delamination (illustrated by the local positive volumetric strain close to the red arrow on Fig. 5a) which did not induce a collapse of the structure. Inside the sample, we do not observe highly negative strains close to the central pore despite the fact that this surface was large enough to facilitate water evaporation. This might be explained by the 50% infill of the printing parameters that created a tortuous central pore, which reduces the drying rate for the parts of the cube in contact with the central part.

We can also observe for t = 0–20 min and for t = 40–60 min negative but also positive local volumetric strains. The local negative strains are located inside the filaments and were mainly induced by their vertical shrinkage. This phenomenon appeared to be more pronounced at the bottom of the sample than at its top. On the opposite, we can observe that the local positive strains are located at the edges of the filament in contact with the central pore and correspond to their horizontal expansion. These two observations explain why the final shape of the filament is oval and not circular, as illustrated in Fig. 3, and already observed in (Klar et al. 2019): as a homogeneous lateral shrinkage was observed during the drying of a single filament, this anisotropic behaviour of the lateral shrinkage upon drying is a combination of diameter reduction due to drying enhanced by the weight of the upper filaments. The lateral expansion that occurs mainly during the first part of the drying is

referred as "collapse" in (Klar et al. 2019). This "collapse" is limited and did not induce a collapse of the structure due to the rheological properties of the paste (Thibaut et al. 2019). We can notice that at the surface of the central pore the volumetric strain is close to 0, showing that this region stabilised first, as these areas were in contact with air and that the "collapse" rate of the filament decreased.

Fianally, for **t** = 120–140 min, we can observe positive large volumetric strains up to 0.12 which corresponds to the zone where delamination took place as illustrated in Fig. 3. Elsewhere, the drying mechanisms modified the structure at a scale that the correlation cannot capture. Namely, capillary effect probably took place during this stage. For **t** > 180 min, the correlation did not reveal any major changes in the global shape of the samples or inside the sample.

Analysis of the porous phase

The 3D images of Fig. 3 exhibit three types of pores (i) a central pore that exists in the CAD model that is the single pore to be expected in the 3D printed part, (ii) inter-filament porous structures (referred as type B pores) that are the pores located in between filaments and (iii) intra-filament pores (referred as type A pores) that are the pores located inside the filaments. The inter-filament porous structures are due to the successive deposition of layer during the printing process whereas the intra-filament ones come from the extrusion process of the filament (Thibault 2020; Markl et al. 2017). Figure 6a represents side and top view of the initial 3D structure: the central, type A and type B pores were labelled in green, red and B blue, respectively. Figure 6b shows a 3D rendering of the inter-filament and intra-filament porous structures where the structural differences between the two types of pores can be observed. These two last types of pores were automatically identified based on their sphericity: inter-filament porous structures exhibited a sphericity smaller than 0.5 whereas intra-filament pores exhibited a sphericity larger than 0.5.

Central pore evolution

Figure 7a represents the temporal evolution of the volume of the central pores, which was normalised by its initial volume. The initial volume of central pore measured in the ROI was 94 mm^3; this is in accordance with the initial volume of the CAD file. On Fig. 7a, we can identify several regimes.

During the first regime (**t** = 0–80 min), the volume of central pores decreases linearly with time. The behaviour of the central pore during the first 80 min of drying can be directly linked to the macroscopic shrinkage of the sample (Fig. 4a).

During the second regime (**t** = 80–20 min), the decrease of the volume of the central part is less pronounced. Compared to the first part of the curve, the rate of the macroscopic shrinkage (Fig. 4a) remains constant which induces a decrease of the height of the central pore. However, we can observe that inter-filament pores, located close to the borders of the central pore (Fig. 7a), opened and joined the major pore. This slowed down the volume decrease of the central pore.

During the third regime (***t*** = 120–160 min), the volume of the central pore is constant. During this time interval, the rate of the macroscopic shrinkage (Fig. 4a) remains constant which induces a decrease of the height of the central pore which is balanced by the opening of some inter-filament pores joining the central pore.

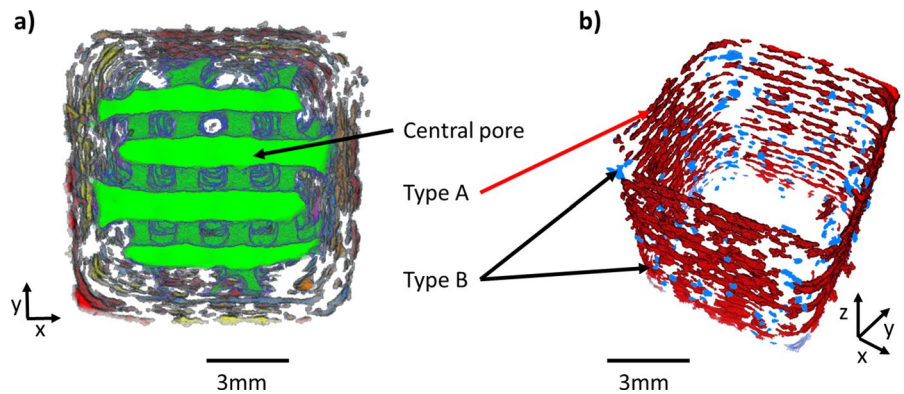

Fig. 6 **a** 3D rendered view of the sample identifying a) central pore (green), **b** type A/intra-filament pores (red) and type B/inter-filaments pores (blue)

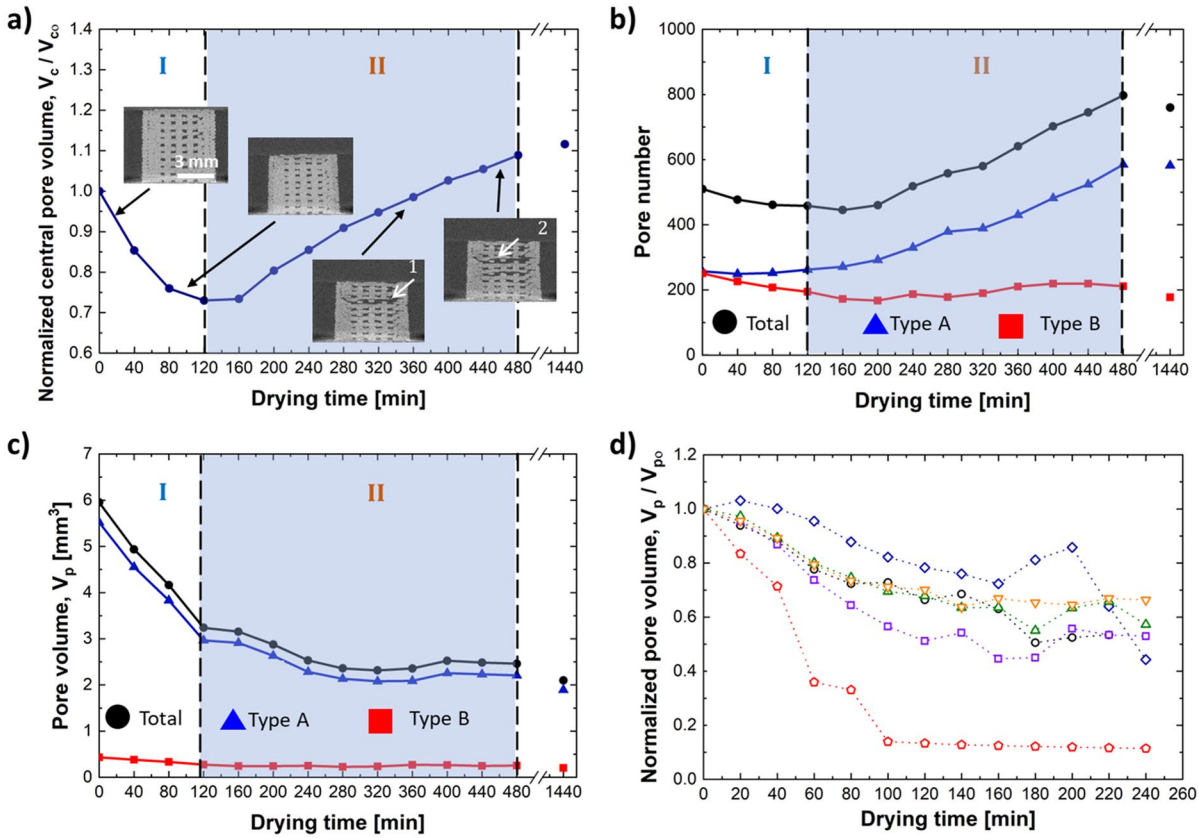

Fig. 7 **a** Temporal evolution of the deformation of the central pore evolution, where $V_{c0} = 94$ mm^3, the arrow 1 and 2 indicates the crack formation and the crack joining, respectively **b** Temporal evolution of the number of inter-filament porous structures (type pore B) and intra-filament pores (type pores A). **c** Temporal evolution of the cumulative volume of inter-filament porous structures (type pore B) and intra-filament of pores (type pores A). **d** Normalised pore volume evolution of 6 tracked inter-filament pores; their initial pore volumes are 0.280, 0.249, 0.138, 0.105, 0.094, 0.049 mm^3 for the pore identified by black circle, red diamond, blue diamond, purple square, green triangle and orange triangle, respectively

During the last regime (**> 160 min),** the volume of the central pore linearly increases. During this time, we do not observe any macroscopic shrinkage, leading to a stabilisation of the main dimensions of the part. The opening of inter-filament pores joining the central pores, as illustrated in Fig. 2, explains the increase of the central pore volume.

Figure 7b and c show the time-evolution of the total number of pores, i.e., the inter-filament (type B) porous structures and the intra-filaments pores (type A), together with the temporal evolution of the volume of these pores, respectively. The inter-filament porous structures represent the higher number of pores and the higher cumulative volume during the whole drying process. Therefore, the temporal evolution of the pores characteristics is mainly driven by the one of the inter-filament porous structures. In addition, Fig. 7b and c show several behaviours.

For t = 0–120 min, the number of inter-filament pores is almost constant whereas their cumulative volume decreased linearly with time. The average size of inter-filament pores decreased from 0.021 to 0.013 mm^3. This 40% decrease in size is confirmed by the tracking of some inter filament pores (Fig. 7d). This comes from the fact that the shrinkage of the structure reduced the space between two filaments (Fig. 5).

For t = 120–480 min, the number of inter-filament pores increased whereas their total volume remained constant. This might be explained by the threshold value applied during the quantification step, as the number of pores is sensitive to the threshold used to identify the pore phase. An analysis of the threshold

values found for each individual scans shows a variation of 3% of the threshold value, which induced in the worst cases a variation of 0.1% on the volume measurements. Moreoever, we can also observe that as the structure dried continuously during the experiment (Fig. 4b), the amount of water decreased, inducing a decrease of about 15% for the grey level of the solid part, this can be quantified for t larger than 140 min. We checked that this decrease in averaged grey level inside the solid phase was not linked to X-ray source instabilities. Therefore, the number of voxels belonging to the porous phase increases inducing, in most cases, larger pores, these larger pores not being excluded due to the threshold on the size of the pores. Moreover, the increase of the number of inter-filament porous structures can also be due to delamination effects. Namely, the global DVC (Fig. 3) in x and y direction do not show any significant variation, meaning that macroscopic aspect of the part did not change anymore, whereas the local DVC (Fig. 6) shows that the filaments, especially inside the structure continued drying, leading to smaller diameter, creating new inter-filament porous structures or increasing their size. On Fig. 7a, we can observe that the modifications due by delamination effect can transform, in very few cases, the intra-filament porous structure into cracks joining the central part.

Figure 7b and c also show that (i) for $t = 0$–160 min, we can observe a linear decrease of the number of intra-filament pores associated with a decrease of the total volume of pores, leading to a decrease of the mean intra-filament pore size. Combining the two graphs shows that these pores have a small volume with an average size in between 0.001 to 0.003 mm^3. The decrease of their numbers might come from the filament shrinkage due to the load of the above layers as observed in Figs. 3 and 6. (ii) for $t > 160$ min, the number of pores increased slowly whereas their cumulative volume remained constant.

What are the microscopic changes during the main phases of the drying regimes?

Figure 8a shows the temporal evolution of the drying rate of the cube deduced from the tomographic data. For the first 240 min, this is in line with results obtained in similar conditions of temperature and humidity as the ones of imaging's room (Thibaut 2020) or found in the literature (Scherer 1990; Thiery et al. 2017; Zhou et al. 2019; Tang and Min 2019, e.g.). For the last 240 min, we observe a steady state regime that is not observed with standard measurements. This comes from the fact that the chosen pixel size is not high enough to capture the details of all the phenomena as a microscale would. Therefore the microstructural description of the drying mechanism is incomplete after 240 min of drying. On this graph, we can observe that the drying rate of the air-dried cube exhibits two main regimes: a constant rate period (~3.510^−5 $gH_2O.h^{-1}.m^{-2}$) (called phase I) that last about 100 min followed a falling rate period (called phase II). These two periods were reported on the graphs representing the temporal evolutions of the microstructural descriptors. Combining the analysis commonly performed and the results presented in Sect. "Results", we can deeper describe the drying mechanisms. For example, the differences observed between the Hencky volumetric strain and the intrinsic volumetric strain come from the heterogeneous drying. This is confirmed by the DVC that shows local heteregenous drying phenomena leading to defects such as delamination. This highlights the effect of the double scale porous geometry of the sample. Morever, the presented results give deeper information regarding the drying mechanisms than the global analysis made up of. For example, during phase I, the main phenomena that occurred aimed at building the rigid skeleton of the dried cube (Metzger 2019; Rémond et al. 2010; Sampson and Yamamoto 2011). Our results show that building the skeleton is associated with a macroscopic anisotropic shrinkage

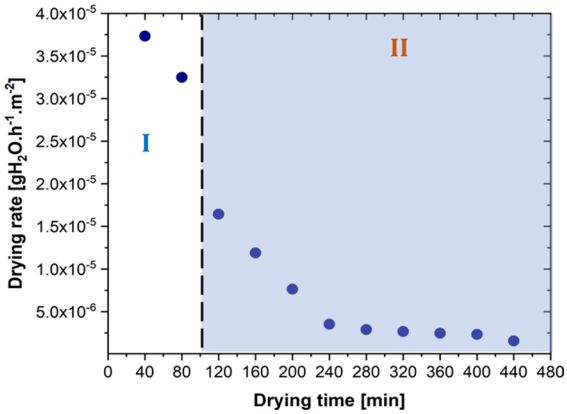

Fig. 8 Temporal evolution of the drying rate

of the structure, a decrease of the solid fraction of the cube, a decrease of the volume of the central pore, a decrease of the number and of the volume of the inter-filament pores and intra-filament porous structures (pores that may evolve to crack), a change of the shape and dimensions of the cross section of filaments. At the beginning of phase II, we observe that the previous changes still took place but at a slower rate. During phase II, most of the changes appears at the filament scale; we observed delamination, an increase of the number of the inter-filament and intra-filament pores. The quantitative analysis captured the last phenomena after the beginning of phase II defined by Fig. 8. Therefore, at the observation scale, a transition zone, that took place between 120 and 160 min of air-drying, might be defined between the two regimes. During this period, it is difficult to define any dominant mechanisms. The length of this transition zone might be explained by 3 factors: (i) it was possible to quantify the evolution that took place up to 30 µm, which is enough to explain part of the microscopic changes but as stated by Metzger (2019) it is complicated to simultaneously image drying phenomena at the three relevant scales on representative samples. (ii) the temperature gradient around the sample modified the drying rate of the sample and might have induced different evolution rates of the 4 faces of the cube; (iii) the CMC dissolved in the water to prepare paste acted as a gelation agent (Edali et al. 2001) and allowed the cellulose fibers to be embedded (Thibaut et al. 2019). This probably modified the drying mechanisms of cellulose fibers and of cellulose fiber mats, compared to the one of paper materials.

Conclusions

The objective of this study was to characterise the macro and mesoscale phenomena that occurred during the drying of a 3D printed sample obtained by extrusion of ligno-cellulosic aqueous paste. We used sub-minute laboratory X-ray microtomography imaging techniques during air drying tests combined with advanced image analysis including DVC to reveal the mechanisms that took place at the macro (sample) scale and at the meso (filament) scale. This allowed to qualitatively and quantitatively analyse structural and kinematical changes to be carry out during the phases of the air drying. During phase I, we quantified the macroscopic anisotropic shrinkage of the structure, the decrease of the solid fraction of the cube, a decrease of the volume of the central pore, a decrease of the number and of the volume of the inter-filament and intra-filament pores, a change of the shape and dimensions of the cross section of filaments. At the beginning of phase II, we observed that the previous changes still took place but at a slower rate. During phase II, most of the changes appeared at the filament scale: we observed delamination effects, an increase of the number of inter-filament and intra-filament pores during the first 8 h. A transition zone was therefore defined during which a competition between the main phenomena taking place during each phase occurred.

It would be interesting to complete these results by performing observations using higher-resolution X-ray images to better define the microstructural changes at the filament scale and therefore better define and quantify the transition zone. Then, these multiscale results would be used to develop models for the prediction of the drying mechanisms of 3D printed parts made up of cellulose and to propose compensation strategies (Thibaut et al. 2020) that will provide final 3D parts closer to the original CAD model.

Acknowledgments 3SR and LGP2 are part of LabEx Tec 21 (ANR-11-LABX-0030) and of Institut Carnot PolyNat (ANR16-CARN-0025). SIMAP is part of LabEx CEMAM (ANR-10-LABX-44-01).

Author contributions PL, LS, AD, LO, DC, DB and SR conceived the study, HM and CT performed the experiment, HM, LS, PL and SR discussed the analysis procedure, HM and SR wrote the manuscript, all the authors analysed the results and revised the manuscript before submission.

Funding The authors acknowledge the financial and scientific support of Université Grenoble Alpes through the IRS Projects “Utilisation du Seuillage en Energie pour une nouvelle Imagerie en Tomographie” and “ Développement de matériaux bio-sourcés fonctionnels pour impression 3D par extrusion”. This work was supported by a grant overseen by the French National Research Agency « Advanced Laboratory X-ray Microtomography» (ANR-18-CE42-0005).

Data availability Available upon request.

Declarations

Conflict of interest None.

Ethics approval Not applicable.

Consent for publication Not applicable.

References

Boulos V, Fristot V, Houzet D, Salvo L, Lhuissier P (2012) Investigating performance variations of an optimized GPU-ported granulometry algorithm. In: Design and Architectures for Signal and Image Processing (DASIP) Conference, Karlsruhe, Germany. pp 1–6

Chalencon F, Orgéas L, Dumont PJJ, Foray G, Cavaillé J-Y, Maire E, Rolland du Roscoat S (2010) Lubricated compression and X-ray microtomography to analyse the rheology of a fibre-reinforced mortar. Rheol Acta 49:221–235. https://doi.org/10.1007/s00397-009-0393-5

Dai L, Cheng T, Duan C, Zhao W, Zhang W, Zou X, Aspler J, Ni Y (2019) 3D printing using plant-derived cellulose and its derivatives: a review. Carbohydr Polym 203:71–86. https://doi.org/10.1016/j.carbpol.2018.09.027

Dewanckele J, Boone MA, Coppens F, Van Loo D, Merkle AP (2020) Innovations in laboratory-based dynamic micro-CT to accelerate in situ research. J Microsc 227(3):197–209. https://doi.org/10.1111/jmi.12879

Dufresne A (2017) Nanocellulose: from nature to high performance tailored materials. Walter de Gruyter GmbH & Co KG, Berlin

Edali M, Esmail MN, Vatistas GH (2001) Rheological properties of high concentrations of carboxymethyl cellulose solutions. J Appl Polym Sci 79(10):1787–1801. https://doi.org/10.1002/1097-4628(20010307)79:10%3c1787::AID-APP70%3e3.0.CO;2-2

Firmanda A, Syamsu K, Sari WY, Cabral J, Pletzer D, Mahadik B, Fisherd J, Fahma F (2021) 3D printed cellulose based product applications. Mater Chem Front 6:254–279. https://doi.org/10.1039/d1qm00390a

Huan S, Ajdary R, Bai L, Klar V, Rojas OJ (2018) Low solids emulsion gels based on nanocellulose for 3D-printing. Biomacromol 20(2):635–644. https://doi.org/10.1021/acs.biomac.8b01224

Joffre T, Isaksson P, Dumont PJJ, Rolland du Roscoat S, Sticko S, Orgéas L, Gamstedt K (2016) A method to measure moisture induced swelling properties of a single wood cell. Exp Mech 56:723–733. https://doi.org/10.1007/s11340-015-0119-9

Klar V, Pere J, Turpeinen T, Kärki P, Orelma H, Kuosmanen P (2019) Shape fidelity and structure of 3D printed high consistency nanocellulose. Sci Rep 9:3822. https://doi.org/10.1038/s41598-019-40469-x

Klar V, Kärki P, Orelma H, Kuosmanen P (2017) Analysis of drying deformation of 3D printed nanocellulose structures. In: Cellulose Materials Doctoral Students Conference 2017. Graz University of Technology, TUG. Retrieved from https://research.aalto.fi/en/publications/analysis-of-drying-deformation-of-3d-printed-nanocellulose-structures(447440d2-bf95-47bb-98ab-f9984beb3f4a).html

Lhuissier P, Bataillon X, Maestre C, Sijobert J, Cabrol E, Bertrand P, Boller E, Blandin JJ, Salvo L, Martin G (2020) In situ 3D X-ray microtomography of laser-based powder-bed fusion (L-PBF)—A feasibility study. Addit Manuf 34:101271. https://doi.org/10.1016/j.addma.2020.101271

Markl D, Zeitler JA, Rasch C, Michaelsen MH, Müllertz A, Rantanen J, Rades T, Bøtker J (2017) Analysis of 3D prints by X-ray computed microtomography and terahertz pulsed imaging. Pharm Res 34:1037–1052. https://doi.org/10.1007/s11095-016-2083-1

Markstedt K, Sundberg J, Gatenholm P (2014) 3D bioprinting of cellulose structures from an ionic liquid. 3D Print Addit Manuf. https://doi.org/10.1089/3dp.2014.0004s

Metzger T (2019) A personal view on pore network models in drying technology. Dry Technol 37(5):497–512. https://doi.org/10.1080/07373937.2018.1512502

Pfister A, Landers R, Laib A, Hübner U, Schmelzeisen R, Mülhaupt R (2004) Biofunctional rapid prototyping for tissue-engineering applications: 3D bioplotting versus 3D printing. J Polym Sci, Part A-1 Polym Chem 42(3):624–638. https://doi.org/10.1002/pola.10807

Rémond R, TurnerIan W, Perre P (2010) Modeling the drying and heat treatment of lignocellulosic biomass: 2D effects due to the product anisotropy. Dry Technol 28:1013–1022. https://doi.org/10.1080/07373937.2010.497093

Sampson WW, Yamamoto J (2011) The drying shrinkage of cellulosic fibres and isotropic paper sheets. J Mater Sci 46:541–547. https://doi.org/10.1007/s10853-010-5006-2

Scherer GW (1990) Theory of drying. J Am Ceram Soc 73(1):3–14. https://doi.org/10.1111/j.1151-2916.1990.tb05082.x

Stamati et al (2020) spam: software for practical analysis of materials. J Open Sour Softw. https://doi.org/10.21105/joss.02286

Tang Y, Min J (2019) Water film coverage model and its application to the convective air-drying simulation of a wet porous medium. Int J Heat Mass Transf 131:999–1008. https://doi.org/10.1016/J.IJHEATMASSTRANSFER.2018.11.094

Thibaut C, Denneulin A, Rolland du Roscoat S, Beneventi D, Orgéas L, Chaussy D (2019) A fibrous cellulose paste formulation to manufacture structural parts using 3D printing by extrusion. Carbohydr Polym 212:119–128. https://doi.org/10.1016/j.carbpol.2019.01.076

Thibaut C (2020) Development of fibrous cellulosic materials for the production of bio-based 3D printed objects by extrusion. PhD thesis, Univ. of Grenoble Alpes, France

Thiery J, Rodts S, Weitz D, Coussot P (2017) Drying regimes in homogeneous porous medium from macro to nano-scale. Phys Rev Fluids 2:07420. https://doi.org/10.1103/PhysRevFluids.2.074201

Viguié J, Dumont PJJ, Mauret E, Rolland du Roscoat S, Vacher P, Desloges I, Bloch J-F (2011) Analysis of the hygroexpansion of a material formed of lignocellulosic fibres by digital correlation. J Mater Sci 46:4756–4769. https://doi.org/10.1007/s10853-011-5386-y

Wainwright SA, Biggs WD, Currey JD (1982) Mechanical design in organisms. Princeton University Press, Princeton

Wang Q, Sun J, Yao Q, Ji C, Liu J, Zhu Q (2018) 3D printing with cellulose materials. Cellulose 25:4275–4301. https://doi.org/10.1007/s10570-018-1888-y

Zhou T, Ioannidou K, Ulm F-J, Bazant MZ, Pellenq RJ-M (2019) Multiscale poromechanics of wet cement paste. Proc Natl Acad Sci 116(22):10652–10657. https://doi.org/10.1073/pnas.1901160116